Dynamic measurement of gas volume fraction in a CO_2 pipeline through capacitive sensing and data driven modelling

Ding Shao[1], Yong Yan[2*], Wenbiao Zhang[1], Shijie Sun[3], Caiying Sun[1], Lijun Xu[3]

1 School of Control and Computer Engineering, North China Electric Power University, Beijing 102206, P.R. China
2 School of Engineering and Digital Arts, University of Kent, Canterbury, Kent CT2 7NT, U.K.
3 School of Instrumentation and Optoelectronic Engineering, Beihang University, Beijing 100191, P.R. China.
* Correspondent author: y.yan@kent.ac.uk

Abstract

Gas volume fraction (GVF) measurement of gas-liquid two-phase CO_2 flow is essential in the deployment of carbon capture and storage (CCS) technology. This paper presents a new method to measure the GVF of two-phase CO_2 flow using a 12-electrode capacitive sensor. Three data driven models, based on back-propagation neural network (BPNN), radial basis function neural network (RBFNN) and least-squares support vector machine (LS-SVM), respectively, are established using the capacitance data. In the data pre-processing stage, copula functions are applied to select feature variables and generate training datasets for the data driven models. Experiments were conducted on a CO_2 gas-liquid two-phase flow rig under steady-state flow conditions with the mass flowrate of liquid CO_2 ranging from 200 kg/h to 3100 kg/h and the GVF from 0% to 84%. Due to the flexible operations of the power generation utility with CCS capabilities, dynamic experiments with rapid changes in the GVF were also carried out on the test rig to evaluate the real-time performance of the data driven models. Measurement results under steady-state flow conditions demonstrate that the RBFNN yields relative errors within ±7% and outperforms the other two models. The results under dynamic flow conditions illustrate that the RBFNN can follow the rapid changes in the GVF with an error within ±16%.

Keywords: Carbon capture and storage; Gas volume fraction; Two-phase CO_2 flow; Data driven models; Copula functions

Nomenclature

τ	Kendall's correlation coefficient	h_g	Specific enthalpy of gas CO_2 before being mixed (kJ/kg)
μ	Spearman's correlation coefficient	h_l	Specific enthalpy of liquid CO_2 before being mixed (kJ/kg)
r	Pearson's correlation coefficient	h_g'	Specific enthalpy of gas CO_2 in two-phase flow (kJ/kg)
α_0	Gas volume fraction without correction	h_l'	Specific enthalpy of liquid CO_2 in two-phase flow (kJ/kg)
χ	Gas mass fraction	ρ_l	Density of liquid CO_2 (kg/m^3)
α	Reference gas volume fraction	ρ_g	Density of gas CO_2 (kg/m^3)
q_{mg}	Mass flowrate of gas CO_2 before being mixed (kg/h)	C_{norm}	Normalized capacitance
q_{ml}	Mass flowrate of liquid CO_2 before being mixed (kg/h)	C_l	Capacitance measured when the pipe is full of liquid CO_2 (fF)
q'_{mg}	Mass flowrate of gas CO_2 in two-phase flow (kg/h)	C_g	Capacitance measured when the pipe is full of gas CO_2 (fF)
q'_{ml}	Mass flowrate of liquid CO_2 in two-phase flow (kg/h)	C_i	Capacitance measured for two-phase CO_2 (fF)

1. Introduction

Global warming and climate change due to greenhouse gas emissions impede the global economic development. The excessive CO_2 emissions from fossil fuel fire power generation utilities is regarded as the main cause of global warming. Recently, carbon capture and storage (CCS) technology has been proposed and is being deployed as an effective approach to reduce the emissions of CO_2 from the power generation (Leung et al., 2014; Kemper, 2015). Accurate measurement of CO_2 flow in pipelines is crucial to economical and safe operations in the CCS process. However, accidental leakage from CO_2 pipelines or small changes of the environmental temperature will lead to a significant change in the phase of CO_2, resulting in gas-liquid two-phase CO_2 flow (Wen et al., 2019; Zhang et al., 2018). Impurities produced using different capture methods may also lead to changes in phase properties of CO_2 flow (Nazeri et al., 2016; Proter et al., 2015). In addition, CCS facilities on fossil fuel fired power plants need to be operated flexibly (Abdilahi et al., 2018, Zhang et al., 2018), such as frequent load changes and rapid start-ups and shutdowns. Due to the complex characteristics of CO_2 flow, accurate measurement of CO_2 fluid parameters is more challenging than other gas-liquid two-phase flows. As an important parameter in two-phase CO_2 flow, the gas volume fraction (GVF) is required to determine the single phase mass flowrate and average density. Therefore, the GVF measurement is essential to

monitor and optimize the operation of the CCS system. However, few studies on the GVF measurement of CO_2 flow have been reported to date.

Several methods based on capacitance probes (Ji et al., 2014;), wire-mesh sensors (Olerni et al., 2013; Bowden et al., 2017), radiation attenuation (Nazemi et al., 2016), optical fiber sensing (Ursenbacher et al., 2004) and ultrasonic sensing (Chakraborty et al., 2009) have been proposed for the direct measurement of the GVF of gas-liquid two-phase flow. In comparison with other measurement instruments, the capacitive sensors have the advantages of low cost, fast response and non-invasiveness (Sun et al., 2017; Sun et al., 2018). Multi-electrode capacitive sensors are often utilized in process tomography to achieve flow pattern recognition and visual monitoring (Xie et al., 2006; Jiang et al., 2009). However, unlike the flow pattern recognition or phase distribution reconstruction of two-phase flow, reconstructed images are usually not required for GVF measurement. Moreover, due to the complex characteristics of gas-liquid two-phase flow, it is difficult to develop a general method that is suitable for all flow patterns.

In recent years, some flow instruments incorporating data driven models, such as artificial neural networks (ANNs) and support vector machine (SVM), have been utilized to achieve GVF measurement under two-phase flow conditions (Figueiredo et al., 2016; Wang et al., 2017; Peyvandi and Rad, 2017; Wang et al., 2018). Data driven models are widely used to represent the hidden relationships in large, complex and multivariate datasets using statistical learning techniques. Wang et al. (2017) proposed several data driven models based on ANNs, SVM and genetic programming to measure both the GVF and liquid mass flowrate of an air-water two-phase flow using Coriolis mass flowmeters (CMFs). Although the mass flow measurement errors are mostly within ±1%, the maximum error of the GVF is still larger than 10%. Peyvandi and Rad (2017) developed an approach by combining gamma ray attenuation with ANNs to measure the GVF of an air-oil-water three-phase flow. Figueiredo et al. (2016) analyzed acoustic attenuation data from an air-oil-water three-phase flow and developed ANNs and least squares support vector machine (LS-SVM) for the GVF measurement and flow pattern recognition. For two-phase CO_2 flow, Wang et al. (2018) combined LS-SVM models and CMFs to measure the GVF in horizontal and vertical pipelines. The relative errors of GVFs both in horizontal and vertical pipelines are within ±10% when the GVFs are larger than 5%. Previous studies have demonstrated that data driven models, especially ANNs and LS-SVM, combined with conventional sensors perform well in the GVF measurement of gas-liquid two-phase flow.

Variable selection is a necessary pre-processing step in the development of data driven models in order to obtain acceptable measurement accuracy. Properties of datasets, including correlation and monotonicity, should be taken into account during data pre-processing. The Pearson's correlation coefficient, which is commonly used to determine statistical dependence, only describes linear dependence (Mu et al., 2018). Recently, copula functions have been used to measure the non-linear dependence and tendency correlation between variables (Han et al., 2019; Karra and Mili, 2019). A series of copula functions, including normal copula, t-copula and Clayton copula, are common choices in the fields of economics, astronomy and meteorology (Mensi et al., 2016; Navarro, 2018; Kim et al., 2019). In comparison to other linear correlation analysis, copula functions can describe both linear and non-linear correlations. For the measurement of gas-liquid two-phase flow, correlations between the sensor signals and two-phase flow parameters are usually non-linear and non-monotonic. Copula functions are capable of providing a comprehensive description of such correlations.

This paper presents a method for the GVF measurement of gas-liquid two-phase CO_2 flow by combining a 12-electrode capacitive sensor and data driven models. Signals from the capacitive sensor are used to develop the measurement models without going through a time-consuming image reconstruction process. During the data pre-processing stage, copula functions are used to establish the non-linear relationships and tendency correlations between the measured capacitance data and the GVF. Three data driven models, including back-propagation neural network (BPNN), radial basis function neural network (RBFNN) and LS-SVM, are established to measure the GVF. Experiments under steady-state flow conditions were conducted on a horizontal pipeline on a CO_2 two-phase flow rig. The performance of the proposed measurement models in this study is evaluated in terms of relative errors. In consideration of the flexible operations of a power generation utility with CCS capability, dynamic experiments with rapid changes in flow conditions were also conducted to assess the real-time performance of the data driven models for GVF measurement.

2. Methodology

2.1. Measurement strategy

The measurement strategy adopted in this study is illustrated in Fig. 1. A high-pressure capacitive sensor is designed and constructed, which consists of 12 identical rectangular electrodes with a length of 40 mm and a width of 7 mm. The electrodes are symmetrically mounted on the exterior of a polytef pipe section with an inner diameter of 25 mm and an outer diameter of 31 mm. More details of the capacitive

sensor are available in Sun et al. (2018). A data acquisition system is developed to measure the capacitances between each pair of electrodes in the sensing head, resulting in a total of 66 (C_{12}^2) independent capacitances. Data driven models, including BPNN, RBFNN and LS-SVM, accept variables from the data acquisition system to infer the GVF of gas-liquid two-phase CO_2 flow.

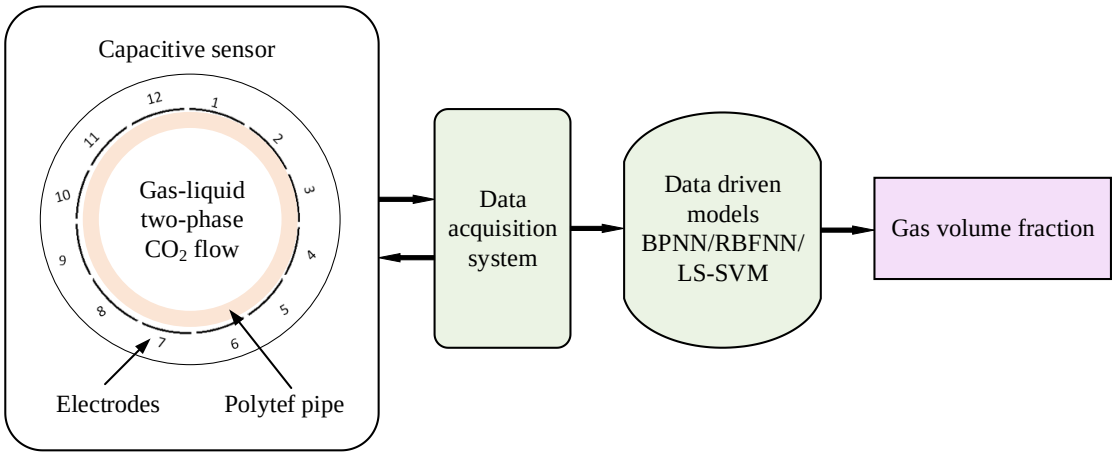

Fig. 1 Overall strategy for the GVF measurement of gas-liquid two-phase CO_2 flow

2.2 Copula function

Selecting an appropriate set of inputs to the data-driven model is a critical step in the GVF measurement. The relationship between the input variables and outputs of the data driven model is usually inferred through statistical analysis. However, the most widely used correlation coefficient in statistics can only analyze and measure the linear relationship between variables. In recent years, copula functions are proposed to describe the dependence of random variables more comprehensively (Han et al., 2019; Karra and Mili, 2019). The copula functions are powerful tools for modeling the non-linear correlation among multiple variables due to their ability of relating the marginal distribution function of each variable to their multivariate joint distributions functions. The distribution functions, including marginal distribution and joint distribution, describe completely the statistical regularity of random variables (Sun et al., 2019). Sklar theory states that a joint distribution can be divided into multiple marginal distributions and a copula function (Sklar, 1959), namely,

$$H\left(x_1, x_2, \cdots, x_n\right) = C\left\{F_1\left(x_1\right), F_2\left(x_2\right), \cdots, F_n\left(x_n\right), \theta\right\} \quad (1)$$

where *H(x)* is the joint distribution function of variables, *F(x)* is the marginal distribution, θ is the correlation degree parameter which can be determined by using the non-parametric kernel density estimation method (Wang et al., 2014), and *C(·)* is the copula function.

Two families of copula functions, *Ellipse-copula* family and *Archimedean-copula* family, have been

applied to describe the relationship between variables. The *Ellipse-copula* family includes normal copula, t-copula and logit copula. Gumbel-copula, Clayton-copula and Frank-copula belong to the *Archimedean-copula* family. The forms of these copula functions can be found in Nelsen (2006). In this paper, a two-dimensional normal copula function is employed to take into account the correlation between each capacitance value and the GVF due to its low computational complexity. For a two-dimensional normal copula function, it can be described as follows:

$$C(u,v)=\frac{1}{2\pi\sqrt{1-r^2}}\int_{-\infty}^{\Phi^{-1}(u)}\int_{-\infty}^{\Phi^{-1}(v)}\exp\left[\frac{-\left(s^2-2rst+t^2\right)}{2\left(1-r^2\right)}\right]dsdt \tag{2}$$

where u and v are two random variables, Φ^{-1} denotes the inverse function of a standard normal distribution function and r denotes the Pearson's correlation coefficient between u and v.

Unlike traditional linear correlation analysis, copula functions can describe both the linear and nonlinear correlations between variables. The most widely used scale-invariant measures of association are the Kendall's and Spearman's rank correlation coefficients (Fredricks and Nelsen, 2007), both of which can be calculated from copula functions:

$$\tau=4\int_0^1\int_0^1 C(u,v)dC(u,v)-1 \tag{3}$$

$$\mu=12\int_0^1\int_0^1 C(u,v)dudv-3 \tag{4}$$

where τ and μ are the Kendall's and Spearman's correlation coefficients, respectively. The Kendall's and Spearman's coefficients are independent of the marginal distribution of random variables. They determine the degree of consistency and remain unchanged after a strict monotonic transformation, which illustrates that these coefficients have wider applicability than linear correlation coefficients.

2.3 Data driven models

In recent years, data driven modeling techniques were proposed for the GVF and flowrate measurement of gas-liquid two-phase flow (Wang et al., 2019; Peyvandi and Rad, 2017). Among these data driven models, the BPNN, RBFNN and LS-SVM have been widely used as alternatives to physical-based and conceptual models. The structure of each data driven model based on BPNN, RBFNN and LS-SVM is explained in detail in this section.

2.3.1 BPNN

As one of the most common neural networks, BPNNs have been applied to achieve the measurement of gas-liquid two-phase flow due to their strong nonlinear mapping capability, good adaptability and

fault tolerance (Azizi et al., 2015). The BPNN is a multilayer neural network consisting of an input layer, an output layer and a hidden layer, as shown in Fig. 2. The output of the BPNN is calculated from:

$$y_{BP}(t)=\sum_{j=1}^{L}\omega_j H_j(t)+b \tag{5}$$

where ω_j and b are the connection weight and bias between the jth hidden neuron and the output layer, respectively. H_j is the output of the jth hidden neurons and is determined from:

$$H_j(t)=f\left(\sum_{i=1}^{n}\omega_{ij}x_i(t)+a_j\right) \tag{6}$$

where ω_{ij} is the connection weight between the ith input neuron and the jth hidden neuron. x_i is the ith input variable and a_j is the bias of jth hidden neuron. $f(x)$ is the activation function of hidden neurons. In this paper, the hyperbolic tangent sigmoid function is used as an activation function of hidden neurons (Figueiredo et al., 2016) and presented by

$$f(x)=\frac{2}{1+e^{-2x}}-1 \tag{7}$$

Although BPNNs have been widely applied in practice, however, a successful BPNN model depends significantly on the user-dependent parameters such as an appropriate model structure and training initialization.

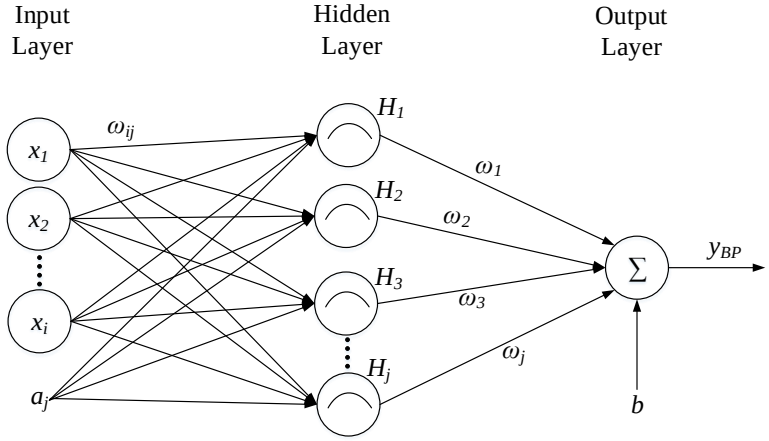

Fig. 2 Structure of a typical BPNN

2.3.2 RBFNN

RBFNN is a feedforward neural network consisting of three layers, as illustrated in Fig. 3, and uses a type of radial basis function (RBF) as activation to the hidden nodes. The output of the network is a linear combination of RBFs of the inputs and neuron parameters. The RBF measures the distance between the input vectors and the weight vectors and is typically taken to be the Gaussian function. The

output of a RBFNN is calculated from:

$$y_{RBF}(t)=\sum_{j=1}^{N}\omega_j(t)\varphi_j\left(x(t)\right) \tag{8}$$

where ω_j is the connection weight between the jth hidden neurons and the output layer, $x(t)$ is the input variables vector, and N is the number of hidden neurons. φ_j is the jth nonlinear mapping between the input neurons and the jth hidden neuron, respectively, namely,

$$\varphi_j\left(x(t)\right)=\exp\left(-\left(\left\|x(t)-C_j\right\|^2/2{\sigma_j}^2\right)\right) \tag{9}$$

where C_j and σ_j^2 is the center vector and the variance for the jth hidden neuron, respectively, and C_j is determined by the K-means clustering method (Liao, 2010).

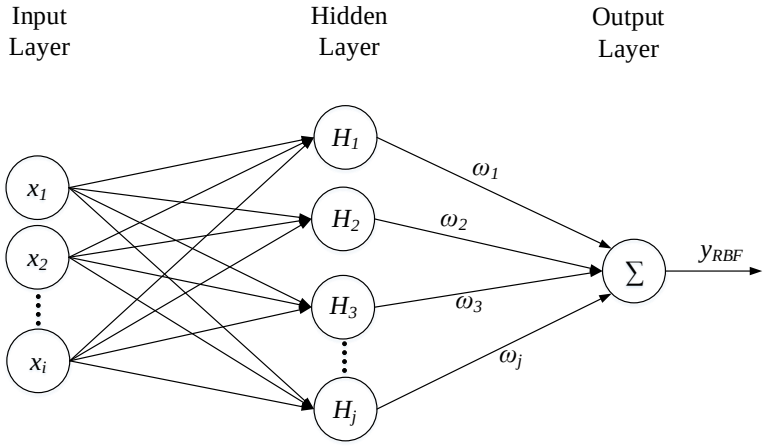

Fig. 3 Structure of RBFNN

2.3.3 LS-SVM

The SVM algorithm maps linear inseparable data to a new space, in which these data become linearly separable. The SVMs have been applied to achieve the phase fraction prediction and flow regime identification due to the good generalization and the suitability for small sample training (Wang et al., 2009; Zhang et al., 2011). In order to achieve faster convergence, Suykens (2002) proposed an LS-SVM model to solve the nonlinear regression problem by mapping the data into a high-dimensional feature space and then developing a linear regression model in this space. Given training samples x and the desired output y, the LS-SVM model is defined as

$$\begin{gathered}\min_{\omega,b,e}\frac{1}{2}\omega^T\omega+\frac{1}{2}\gamma\sum_{k=1}^{n}e \\ s.t. \\ y=\omega^T\varphi(x)+b+e\end{gathered} \tag{10}$$

where ω^T and b are the transposed vector and bias, respectively. $\varphi(x)$ is a nonlinear mapping function.

202 γ refers to penalty parameter. e_k is slack variables. x_k and y_k are the kth input and output elements,
203 respectively.

204 In order to achieve the optimization solution of Eq. 10, Lagrange function is adopted, i.e.

205 $$L(\omega,b,e,a)=\frac{1}{2}\omega^T\omega+\frac{1}{2}\gamma\sum_{k=1}^{n}e_k^2-\sum_{k=1}^{n}a_k\left(\omega^T\varphi(x_k)+b-e_k-y_k\right) \tag{11}$$

206 where a_k is the Lagrange multiplier.

207 Furthermore, the partial derivative of Lagrange function is given by:

208 $$\begin{cases}\dfrac{\partial L}{\partial\omega}=0\rightarrow\omega=\sum_{k=1}^{n}a_k\varphi(x_k)\\ \dfrac{\partial L}{\partial b}=0\rightarrow\sum_{k=1}^{n}a_k=0\\ \dfrac{\partial L}{\partial e_k}=0\rightarrow a_k=\gamma e_k\\ \dfrac{\partial L}{\partial a_k}=0\rightarrow y_k=\omega^T\varphi(x_k)+b+e_k\end{cases} \tag{12}$$

209 The estimation of the LS-SVM model is obtained by solving the following equation,

210 $$y_k=\sum_{k=1}^{n}a_kK(x,x_k)+b \tag{13}$$

211 where $K(x, x_k)$ is a kernel function.

212 Samples from the original space are mapped into a higher-dimensional space by the kernel functions,
213 such as linear, polynomial, RBF, and sigmoid function. In this study, an RBF kernel function is chosen
214 due to the strong nonlinear mapping abilities. Thus, the output of the LS-SVM model is finally
215 represented as:

216 $$y_{SVM}(t)=\sum_{k=1}^{n}a_k\exp\left(-\frac{1}{2\sigma^2}\left\|x(t)-x_i\right\|^2\right)+b \tag{14}$$

217 **3. Experimental conditions**

218 *3.1 Test rig*

219 Experiments were conducted on a 1-in bore gas-liquid two-phase CO_2 flow rig as depicted in Fig. 4.
220 The capacitive sensor, as shown in Fig. 5, is installed in the horizontal test section. A stainless steel pipe
221 is wrapped outside the polytef pipe to withstand the high pressure. For experiments under steady-state
222 flow conditions, the mass flowrate of liquid CO_2 is set from 200 kg/h to 3100 kg/h, resulting in the
223 reference GVF from 0% to 84%. Experiments under dynamic conditions were also conducted to
224 investigate the real-time performance of the established data driven models. The gas phase CO_2 was

increased from 120 kg/h to 400 kg/h and then decreased from 400 kg/h to 120 kg/h when the liquid phase CO_2 was fixed at 1500 kg/h. Meanwhile, the liquid phase CO_2 was increased from 350 kg/h to 750 kg/h and then decreased from 750 kg/h to 350 kg/h when the gas phase CO_2 was fixed at 70 kg/h. These dynamic flow conditions result in variations in GVF. The material properties and operation conditions of the CO_2 flow test rig are summarized in Table 1.

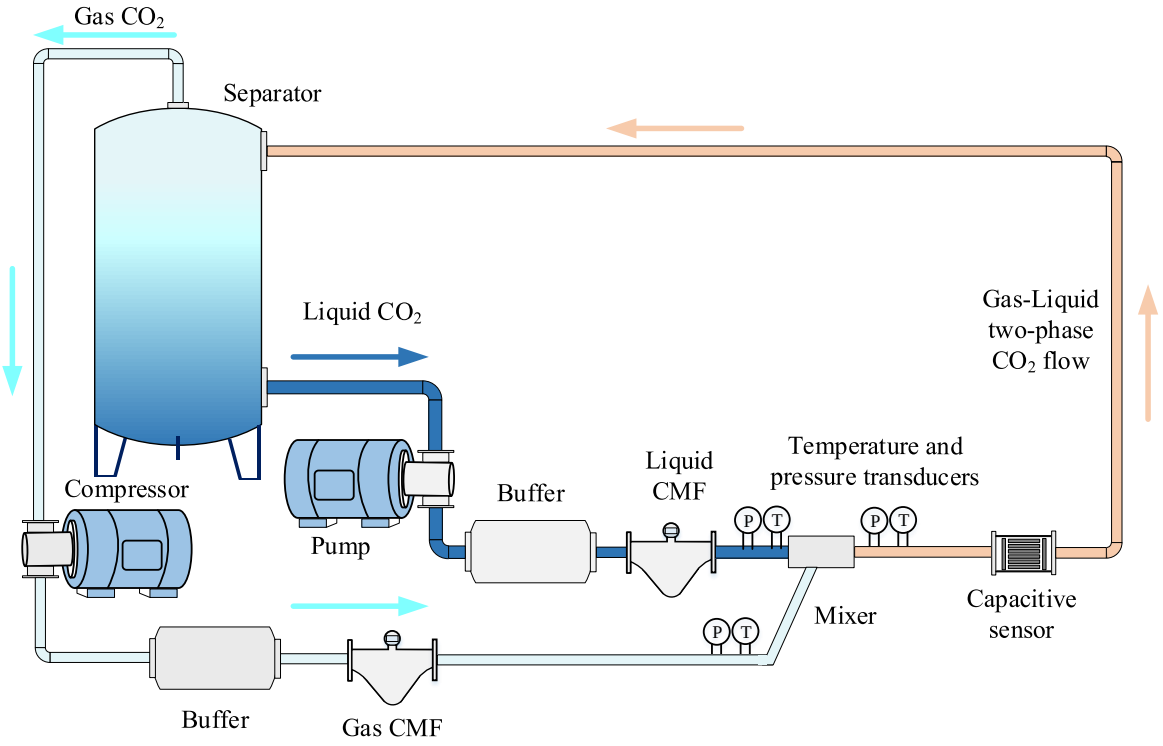

Fig. 4 Schematic of the gas-liquid two-phase CO_2 flow rig

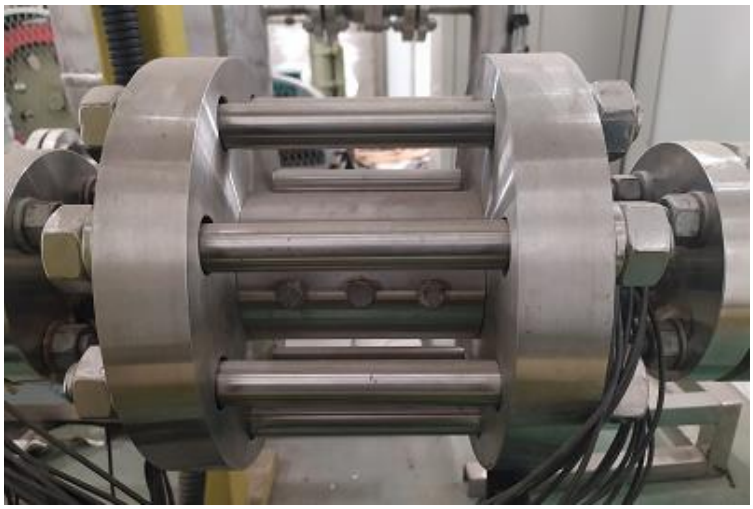

Fig. 5 Photograph of the capacitive sensor

Table 1 Material properties and operation conditions of the CO_2 flow test rig

Parameter	Value	Parameter	Value
Pressure (bar)	57 - 72	Liquid density (kg/m^3)	740 - 800
Temperature (°C)	20 - 30	Gas specific enthalpy (kJ/kg)	403.26 - 437.74
Gas mass flowrate (kg/h)	15 - 400	Liquid specific enthalpy (kJ/kg)	253.25 -262.93
Liquid mass flowrate (kg/h)	70 - 3100	Gas permittivity	1.0
Gas density (kg/m^3)	190 -210	Liquid permittivity	1.6

3.2 Calculation of reference GVF

Two CMFs are installed on the liquid phase and gas phase sections, respectively, to provide the mass flowrate and density of single-phase CO_2 flow. The measurement uncertainty of gas phase CO_2 flow is 0.35% while that of liquid phase CO_2 flow is 0.16%. Temperature and pressure transducers are installed at the entrance and exit of the mixer, respectively, to provide temperature and pressure information of single-phase and two-phase CO_2 flows. When the gas and liquid CO_2 are mixed without considering the phase transition between the two, the GVF (α_0) of two-phase CO_2 flow is calculated from,

$$\alpha_0 = \frac{q_{mg}\rho_l}{q_{ml}\rho_g + q_{mg}\rho_l} \tag{15}$$

where q_{mg} and ρ_g are the mass flowrate and density of gas phase CO_2, respectively. q_{ml} and ρ_l are the mass flowrate and density of liquid phase CO_2, respectively. These parameters are all obtained from the reference CMFs.

However, phase transition may occur due to the changes in temperature and pressure at the mixer. The GVF should be corrected by the first law of thermodynamics of an open system as follows:

$$\begin{aligned} q_{mg}h_g + q_{ml}h_l &= q'_{mg}h'_g + q'_{ml}h'_l \\ q_{mg} + q_{ml} &= q'_{mg} + q'_{ml} \end{aligned} \tag{16}$$

where h_g and h_l are the specific enthalpy values of pure gas and liquid CO_2 before being mixed, respectively. h_g' and h_l' are the specific enthalpy values of gas and liquid CO_2 in two-phase flow, respectively. q'_{mg} and q'_{ml} are the mass flowrate of gas and liquid CO_2 in two-phase flow, respectively. Specific enthalpy is a thermodynamic quantity equivalent to internal energy of a system plus the product of its pressure and volume. Temperatures and pressures at the entrance and exit of the mixer are used to determine the specific enthalpy of CO_2. The gas mass fraction (χ) and the reference GVF (α) are calculated as follows,

$$\chi = \frac{\left(h_l - h_l^{'}\right) - \frac{q_{ml}}{q_{ml} + q_{mg}}\left(h_l - h_g\right)}{h_g^{'} - h_l^{'}} \tag{17}$$

$$\alpha = \frac{\chi \rho_l}{(1-\chi)\rho_g} \tag{18}$$

4. Results and Discussion

4.1 Correlation analysis by copula functions

Firstly, the measured capacitances are normalized as follows,

$$C_{norm} = \frac{C_i - C_l}{C_g - C_l} \tag{19}$$

where C_i is the capacitance measured under two-phase CO_2 flow conditions. C_l and C_g are the capacitances which are measured during calibration when the pipeline is full of liquid phase CO_2 and gas phase CO_2, respectively.

Secondly, marginal probability density distributions for the capacitances of each pair of electrodes are estimated using the non-parametric kernel density estimation method. Joint distributions between the measured capacitances and GVFs are established by using normal copula functions and the semi-parametric pseudo-maximum-likelihood method. Finally, the Kendall's and Spearman's rank correlation coefficients between the capacitance values and the GVFs are calculated from Eq. 3 and Eq. 4.

Tables 2 and 3 summarize the Kendall's and Spearman's correlation coefficients calculated from copula functions. The closer these coefficients get to 1 (or -1), the stronger the positive (or negative) correlation is. The top 20% variables with the strongest correlation are selected and their distributions are depicted in Fig. 6.

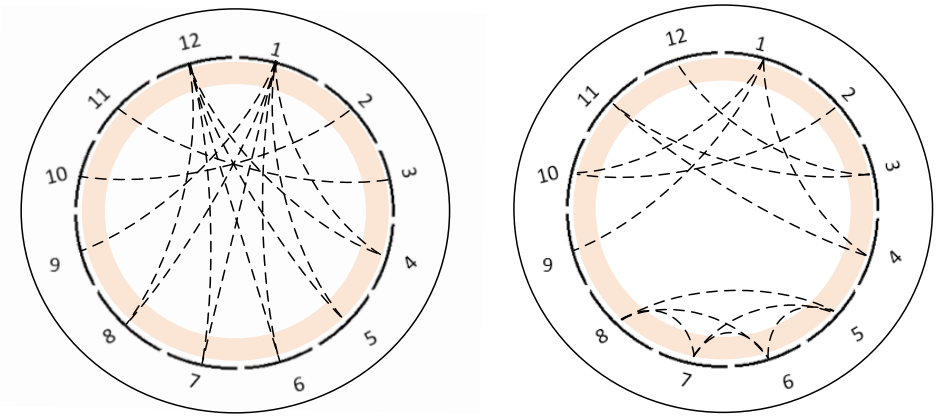

(a) (b)

Fig. 6 Distributions of electrode pairs selected by different coefficients. (a) Kendall's coefficient (b) Spearman's coefficient.

From Fig. 6 (a), electrodes selected by Kendall's coefficient are mainly distributed in the top and bottom of the horizontal pipeline. The sensing area of these electrodes covers the entire interior of the pipe which is good to obtain sufficient information about the flow. However, the sensing segments of the electrode pairs selected by Spearman's coefficients are located at the edge of the pipeline as shown in Fig. 6 (b). To obtain complete assessment for input variables, capacitances selected by both Kendall's and Spearman's coefficients are used to develop data driven models. The performances of these models are evaluated and compared in terms of relative errors.

Table 2 Kendall's coefficients between the GVFs and capacitances

Number of electrodes	2	3	4	5	6	7	8	9	10	11	12
1	0.32	0.78	**0.92**	**0.92**	**0.92**	**0.92**	**0.93**	**0.94**	0.85	0.38	0.7
2	--	0.63	0.76	0.77	0.76	0.77	0.78	**0.89**	0.75	0.58	0.34
3	--	--	0.55	0.57	0.58	0.59	0.6	0.61	0.66	0.83	0.82
4	--	--	--	0.87	0.85	0.31	0.27	0.18	0.56	0.88	**0.91**
5	--	--	--	--	0.82	0.79	0.68	0.31	0.55	0.87	**0.9**
6	--	--	--	--	--	0.73	0.8	0.35	0.54	0.86	**0.89**
7	--	--	--	--	--	--	0.81	0.37	0.53	0.86	**0.89**
8	--	--	--	--	--	--	--	0.4	0.52	0.86	**0.89**
9	--	--	--	--	--	--	--	--	0.49	0.86	**0.89**
10	--	--	--	--	--	--	--	--	--	0.67	0.78
11	--	--	--	--	--	--	--	--	--	--	0.23

Table 3 Spearman's coefficients between the GVFs and capacitances

Number of electrodes	2	3	4	5	6	7	8	9	10	11	12
1	0.3	0.69	**0.86**	0.75	0.75	0.76	0.78	**0.79**	**0.82**	0.22	0.77
2	--	0.49	0.72	0.72	0.72	0.73	0.74	0.75	**0.78**	0.46	0.19
3	--	--	0.27	0.31	0.33	0.35	0.37	0.38	0.47	**0.79**	**0.78**
4	--	--	--	0.63	0.6	0.56	0.52	0.42	0.31	**0.78**	0.72
5	--	--	--	--	**0.88**	**0.87**	**0.84**	0.56	0.29	0.77	0.7
6	--	--	--	--	--	**0.88**	**0.87**	0.6	0.27	0.76	0.69
7	--	--	--	--	--	--	**0.86**	0.64	0.25	0.76	0.68
8	--	--	--	--	--	--	--	0.67	0.22	0.76	0.68
9	--	--	--	--	--	--	--	--	0.17	0.76	0.69
10	--	--	--	--	--	--	--	--	--	0.52	0.68
11	--	--	--	--	--	--	--	--	--	--	0.15

293 *4.2 Performance of data driven models*

294 *4.2.1 Steady-State flow conditions*

295 A total of 197 sets of the capacitance data under steady-state flow conditions were acquired as sample
296 data for training BPNN, RBFNN and LS-SVM, among which 158 sets (80% of the data) are adopted
297 as training data. The remaining 39 sets (20% of the data) are used as testing data. The three data driven
298 models are compared in terms of measurement accuracy.

299 Fig. 7 shows a comparison between the reference GVF and measured GVF from the data driven models
300 using variables selected using the Kendall's coefficient. The relative errors from the BPNN and LS-
301 SVM models are within ±13% and ±12%, respectively, whilst the RBFNN model yields a relative error
302 within ±7%. The RBFNN is remarkably more accurate than BPNN and LS-SVM due probably to the
303 fact that the K-means clustering of input variables during the training of the RBFNN model has similar
304 effect on the flow pattern classification of two-phase CO_2 flow.

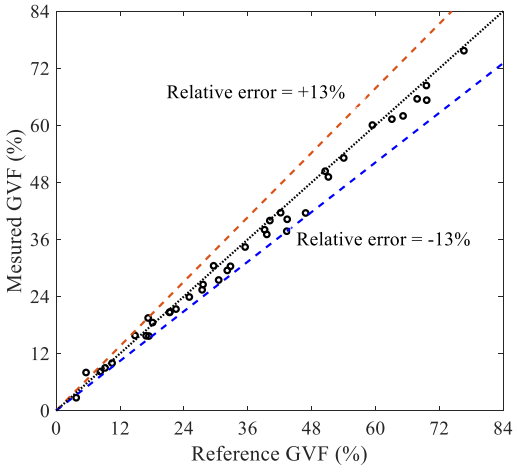

305
306 (a)

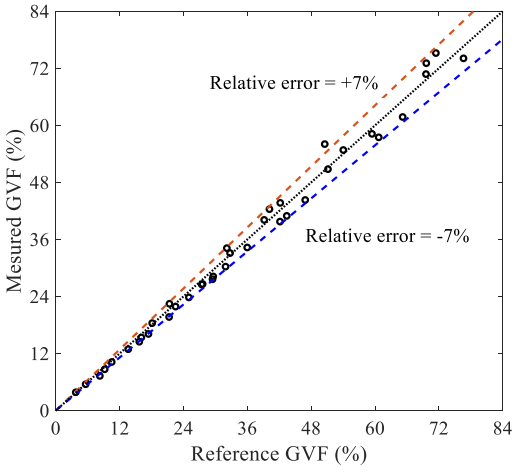

(b)

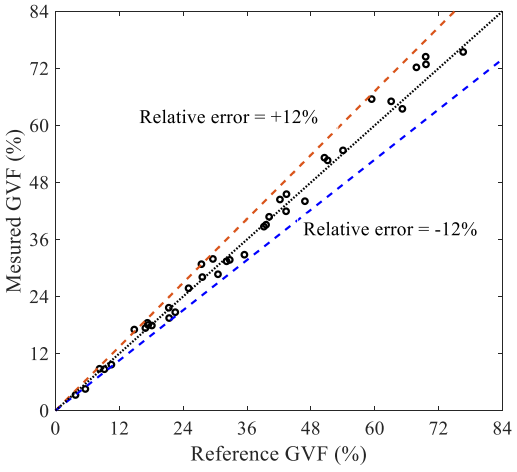

307
308 (c)

Fig. 7 Comparison between the measured GVF and reference GVF using variables selected via the Kendall's coefficient. (a) BPNN. (b) RBFNN. (c) LS-SVM.

Fig. 8 depicts the comparison between the reference GVF and measured GVF using variables selected via the Spearman's coefficient. The relative errors of the BPNN, RBFNN and LS-SVM models are within ±18%, ±13.8% and ±17%, respectively. The mathematical formulations of Kendall's and Spearman's coefficients are different, resulting in different selected variables and outputs of the data driven models. However, according to Fig. 7 and Fig. 8, both coefficients are effective in selecting input variables for the data driven models. It is because that both coefficients are developed to determine the degree of consistency, which means they are both effective in measuring the nonlinear correlation between the measured capacitance data and GVF. However, the measurement area of electrode pairs selected via Spearman's coefficient is mostly located at the edge of the pipeline, some information about the fluid in the center of the pipeline may be lost, resulting in lower accuracy than that in Fig. 7 for all three models.

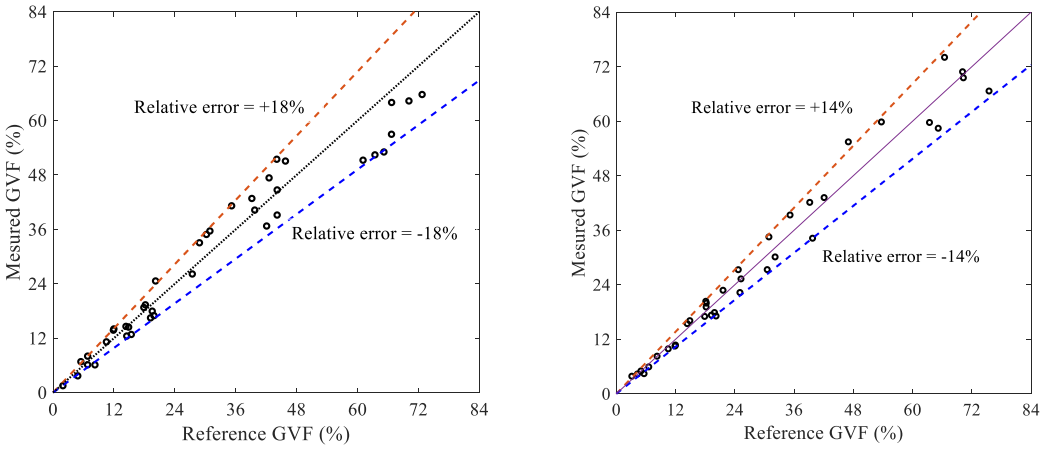

(a)

(b)

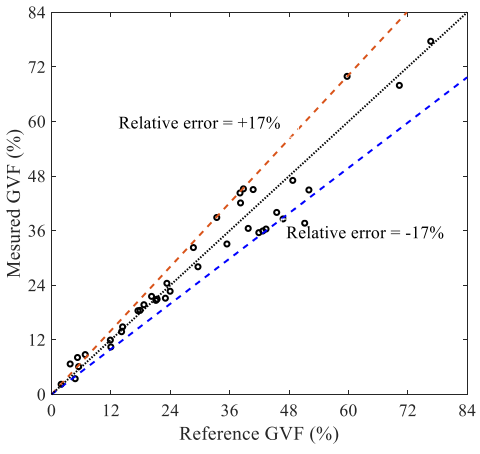

(c)

Fig. 8 Comparison between the measured GVF and reference GVF using variables selected via the Spearman's coefficient. (a) BPNN. (b) RBFNN. (c) LS-SVM.

Fig. 9 and Fig. 10 illustrate the relative error histograms from the data driven models using the two different variable selection methods. It is clear that the error distributions of the BPNN and RBF models are much wider and dispersive than those of RBFNN. By comparing the relative errors and error distributions from data driven models, we can conclude that the measurement results from RBFNN incorporating copula functions produce the lowest relative errors and the highest concentration of the error distributions.

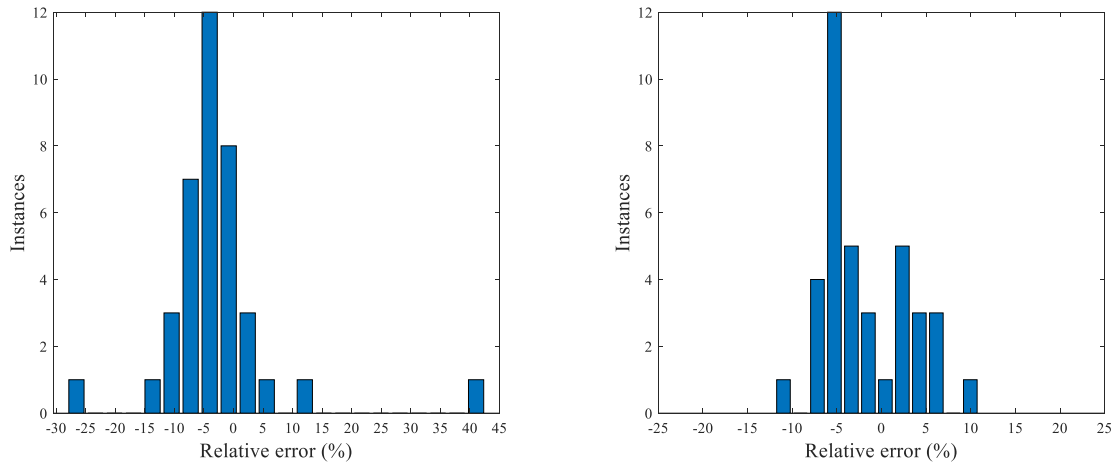

(a) (b)

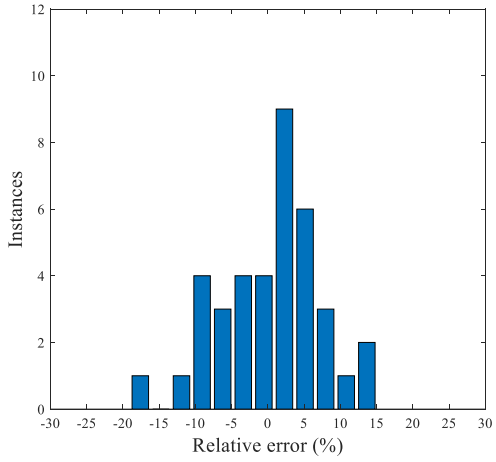

(c)

Fig. 9 Relative error histograms of BPNN, RBFNN and LS-SVM using variables selected by the Kendall's coefficient. (a) BPNN. (b) RBFNN. (c) LS-SVM.

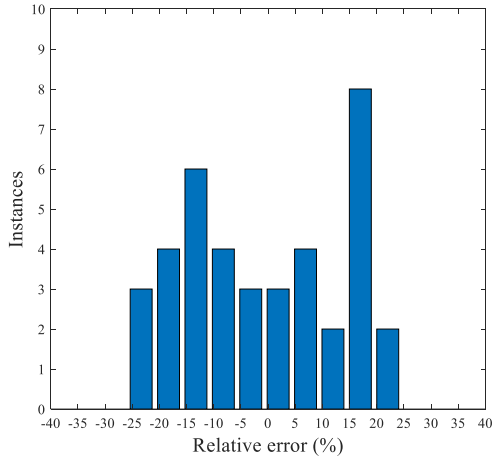

(a)

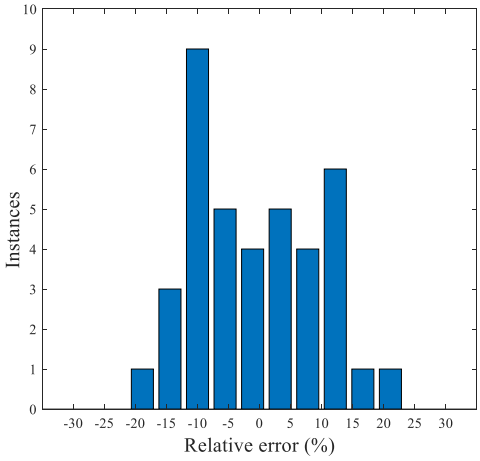

(b)

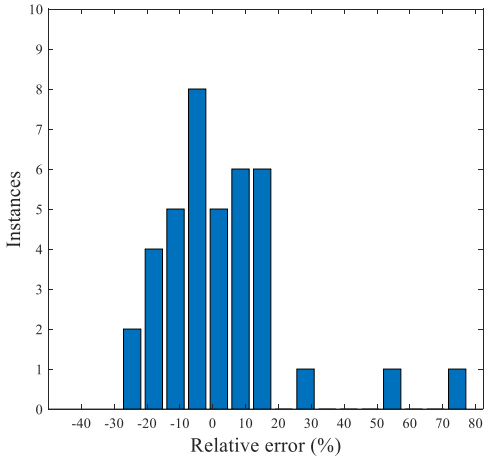

(c)

Fig. 10 Relative error histograms of BPNN, RBFNN and LS-SVM using variables selected by the Spearman's coefficient. (a) BPNN. (b) RBFNN. (c) LS-SVM.

4.2.2 Dynamic conditions

The RBFNN, which outperforms the BPNN and LS-SVM under steady-state flow conditions, is applied to achieve the GVF measurement under dynamic conditions. Fig. 11 shows the measurement performance of the RBFNN during the dynamic operations in the horizontal test section. As shown in Fig. 11 (a) and (b), the mass flowrate of gas phase was fixed at 70 kg/h while the mass flowrate of liquid phase experienced the step increase and decrease. In comparison with the reference GVF, the measured GVF can follow the transient changes. Fig. 11 (c) and (d) show the transient behaviours with increasing and decreasing gas phase CO_2 while the liquid phase was fixed at 1500 kg/h. The measurement results can also follow the trend of reference GVF. However, as shown in Fig. 11 (d), the reduction in GVF is gradual because the inertia of the compressor at a reduced frequency is larger than that at an increased

356 frequency, which prevents step reduction in the mass flowrate of gas phase CO_2. Meanwhile, the buffer
357 installed behind the compressor serves to keep the mass flowrate of gas CO_2 stable in the pipeline,
358 which also prevents step change in the gas phase CO_2 under dynamic conditions. A comparison between
359 the reference GVF and measured GVF during dynamic conditions is plotted in Fig. 12. It is clear that
360 the relative errors are within ±16% in all four cases.

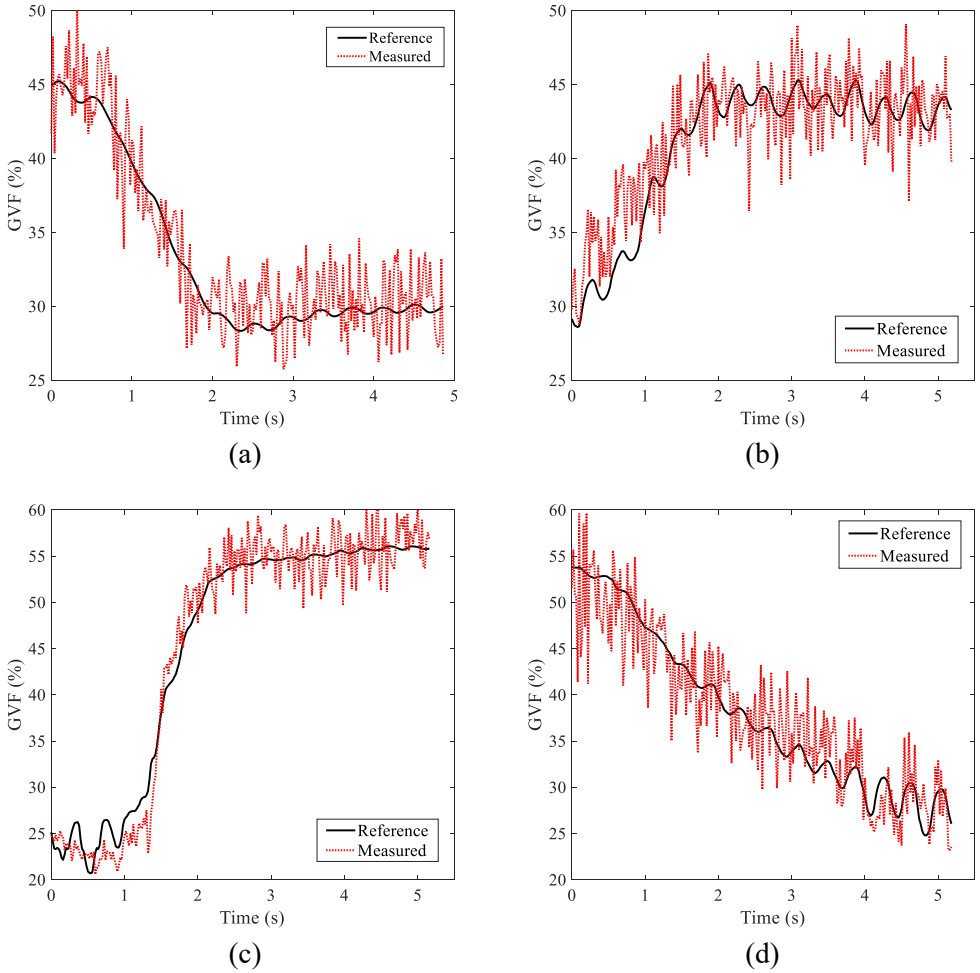

361
362
363
364

365 Fig. 11 Measuremnet performance of RBFNN under dynamic conditions. (a) Increasing liquid CO_2
366 with fixed gas CO_2. (b) Decreasing liquid CO_2 with fixed gas CO_2. (c) Increasing gas CO_2 with fixed
367 liquid CO_2. (d) Decreasing gas CO_2 with fixed liquid CO_2.

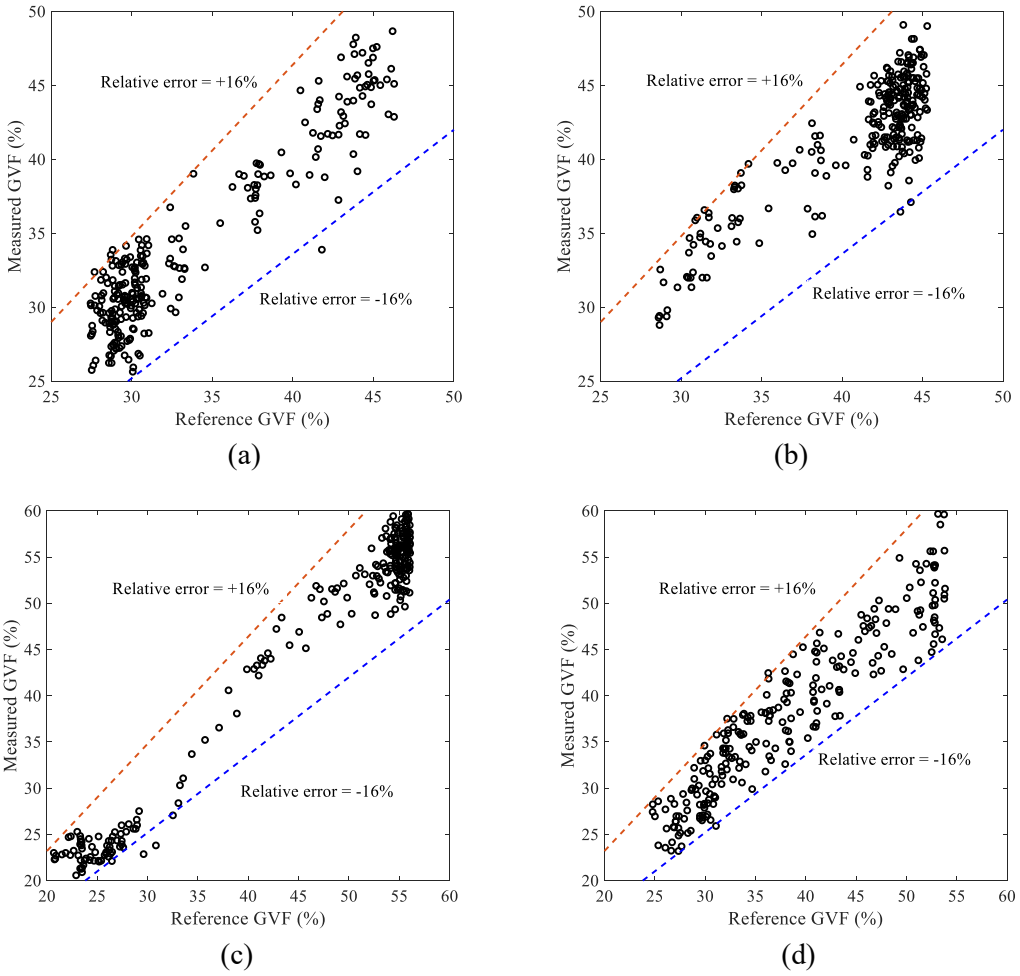

Fig. 12 Comparison between the measured GVF and reference GVF under dynamic conditions. (a) Increasing liquid CO_2 with fixed gas CO_2. (b) Decreasing liquid CO_2 with fixed gas CO_2. (c) Increasing gas CO_2 with fixed liquid CO_2. (d) Decreasing gas CO_2 with fixed liquid CO_2.

5. Conclusions

In this paper analytical and experimental investigations have been carried out to achieve the GVF measurement of gas-liquid two-phase CO_2 flow using a 12-electrode capacitive sensor and data driven models. The results have shown that the RBFNN model produces more accurate GVF measurement than the BPNN and LS-SVM models. During the data pre-processing stage, copula functions and two rank correlation coefficients, i.e. Kendall's and Spearman's coefficients, have been used to select input variables for the data driven models. Under steady-state flow conditions the RBFNN yields a relative error within ±7% in the horizontal pipeline for the GVF ranging from 0% to 84%, whilst the BPNN and LS-SVM models give relative errors within ±13% and ±12%, respectively. The results under dynamic flow conditions have verified the real-time performance of the RBFNN with a relative error within ±16%. It should be stressed that the GVF measurement of the two-phase CO_2 flow using the capacitance

signals and data driven models is achieved without the time-consuming image reconstruction algorithms.

Acknowledgements

The authors wish to acknowledge the National Natural Science Foundation of China (No.61973113) and the financial support of the UK CCS Research Centre (www.ukccsrc.ac.uk). The UK CCSRC is funded by the EPSRC as part of the RCUK Energy Programme.

References

Abdilahi, A.M., Mustafa, M.W., Abujarad, S.Y., Mustapha, M., 2018. Harnessing flexibility potential of flexible carbon capture power plants for future low carbon power systems: Review. Renew. Sust. Energ. Rev. 81, 3101-3110.

Azizi S., Awad M. M., Ahmadloo E., 2015. Prediction of water holdup in vertical and inclined oil-water two-phase flow using artificial neural network. Int. J. Multiph. Flow 80:181-187.

Bowden, R.C., Lessard, étienne, Yang, S.K., 2017. Void fraction measurements of bubbly flow in a horizontal 90 degree bend using wire mesh sensors. Int. J. Multiph. Flow 99, 30-47.

Chakraborty, S., Keller, E., Talley, J., Srivastav, A., Ray, A., Kim, S., 2009. Void fraction measurement in two-phase flow processes via symbolic dynamic filtering of ultrasonic signals. Meas. Sci. Technol. 20(2), 023001.

Figueiredo, M. M. F., Goncalves, J. L., Nakashima, A. M. V., Fileti, A. M. F., Carvalho, R. D. M., 2016. The use of an ultrasonic technique and neural networks for identification of the flow pattern and measurement of the gas volume fraction in multiphase flows. Exp. Therm. Fluid Sci. 70, 29-50.

Fredricks, G. A., Nelsen, R. B., 2007. On the relationship between Spearman's rho and Kendall's tau for pairs of continuous random variables. J. Stat. Plan. Infer. 137(7), 2143-2150.

Han, S., Qiao, Y., Yan, J., Liu, Y., Li, L., Wang, Z., 2019. Mid-to-long term wind and photovoltaic power generation prediction based on copula function and long short term memory network. Appl. Energy 239, 181-191.

Ji, H., Chang, Y., Huang, Z., Wang, B., Li, H., 2014. Voidage measurement of gas–liquid two-phase flow based on capacitively coupled contactless conductivity detection. Flow Meas. Instrum. 40, 199-205.

Jiang, F., Liu, S., Liu, J., Wang, X., 2009. Measurement of Ice Movement in Water Using Electrical

Capacitance Tomography. J. Therm. Sci. 18(1), 8-12.

Karra, K., Mili, L., 2019. Copula index for detecting dependence and monotonicity between stochastic signals. Inf. Sci. 485, 18-41.

Kemper, J., 2015. Biomass and carbon dioxide capture and storage: A review. Int. J. of Greenh. Gas Control 40, 401-430.

Kim, G., Silvapulle, M.J., Silvapulle, P., 2007. Comparison of semiparametric and parametric methods for estimating copulas. Comput. Stat. Data Anal. 51(6): 2836-2850.

Kim, J.M.; Lee, N., Xiao, X.Y., 2019. Directional dependence between major cities in China based on copula regression on air pollution measurements. PLoS One 14(3), e0213148.

Leung, D.Y.C., Caramanna, G., Maroto-Valer, M.M., 2014. An overview of current status of carbon dioxide capture and storage technologies. Renew. Sust. Energ. Rev. 39, 426–443.

Liao, C., 2010. Genetic k-means algorithm based RBF network for photovoltaic MPP prediction. Energy 35(2), 529-536.

Mensi, W., Hammoudeh, S., Shahzad, S.J.H., Shahbaz, M., 2016. Modelling systemic risk and dependence structure between oil and stock markets using a variational mode decomposition-based copula method. J. Bank Financ. 75, 258-279.

Mu, Y., Liu, X., Wang, L., 2018. A Pearson's correlation coefficient based decision tree and its parallel implementation. Inf. Sci. 435, 40-58.

Navarro, J., 2018. Distribution-free comparisons of residual lifetimes of coherent systems based on copula properties. Stat. Pap. 59(2), 781-800.

Nazemi, E., Feghhi, S.A.H., Roshani, G.H., Peyvandi, R.G., Setayeshi, S., 2016. Precise void fraction measurement in two-phase flows independent of the flow regime using gamma-ray attenuation. Nucl. Eng. Technol. 48(1), 64-71.

Nazeri, M., Maroto-Valer, M.M., Jukes,E., 2016. Performance of coriolis flowmeters in CO_2 pipelines with pre-combustion, post-combustion and oxyfuel gas mixtures in carbon capture and storage. Int. J. of Greenh. Gas Control 54, 297-308.

Nelsen, R.B., 2006. An introduction to Copulas, second ed. Springer Verlag, New York.

Olerni, C., Jia, J., Wang, M., 2013. Measurement of air distribution and void fraction of an upwards air–water flow using electrical resistance tomography and a wire-mesh sensor. Meas. Sci. Technol.

24(3), 035403.

Peyvandi, R.G., Rad, S.Z.I., 2017. Application of artificial neural networks for the prediction of volume fraction using spectra of gamma rays backscattered by three-phase flows. Eur. Phys. J. Plus 132(12), 511.

Porter, R.T.J., Fairweather, M., Pourkashanian, M., Woolley, R.M., 2015. The range and level of impurities in CO_2 streams from different carbon capture sources. Int. J. of Greenh. Gas Control 36, 161-174.

Ren, C., An, N., Wang, J., Li, L., Hu, B., & Shang, D., 2014. Optimal parameters selection for BPNN based on particle swarm optimization: a case study of wind speed forecasting. Knowledge-Based Syst. 56, 226-239.

Schweizer, B., Sklar, A., 1983. Probabilistic metric spaces. New York, North-Holland.

Sklar A., 1959. Fonctions de repartition à n dimensions et leurs marges. Publ. Inst. Statist. Univ. Paris 8, 229-231.

Sun, B., Cao, Y., Feng, Q., Qian, C., Ren, Y., Yang, DZ., 2019. An Archimedean Copula Function-Based Prediction Method for High-Power White LED Considering Multi-Performance. IEEE Trans. Electron. Devices 66(8), 3405-3410.

Sun, S., Cao, Z., Huang, A., Xu, L., Yang, W., 2017. A high-speed digital electrical capacitance tomography system combining digital recursive demodulation and parallel capacitance measurement. IEEE Sens. j. 17, 6690-6698.

Sun, S.J., Zhang, W.B., Sun, J.T., Cao Z., Xu, L.J. Yan, Y., 2018. Real-time imaging and holdup measurement of carbon dioxide under CCS conditions using electrical capacitance tomography. IEEE Sens. J. 18, 7551-7559.

Suykens, Johan A. K., 2002. Least squares support vector machines. Int. J. Circuit Theory Appl. 27(6):605-615.

Ursenbacher, T., Wojtan, L., Thome, J.R., 2004. Interfacial measurements in stratified types of flow. part I: new optical measurement technique and dry angle measurements. Int. J. Multiph. Flow 30(2), 107-124.

Wang, H. X., Zhang, L. F., 2009. Identification of two-phase flow regimes based on support vector machine and electrical capacitance tomography. Meas. Sci. Technol. 20(11), 114007.

473 Wang, L., Liu, J., Yan, Y., Wang, X., Wang, T., 2017. Gas-liquid two-phase flow measurement using
474 Coriolis flowmeters incorporating artificial neural network, support vector machine, and genetic
475 programming algorithms. IEEE Trans. Instrum. Meas. 66(5), 852-868.
476 Wang, L., Yan, Y., Wang, X., Wang, T., Duan, Q., Zhang, W., 2018. Mass flow measurement of gas-
477 liquid two-phase CO_2 in CCS transportation pipelines using Coriolis flowmeters. Int. J. of Greenh.
478 Gas Control 68, 269-275.
479 Wang, S., Wang, J., Chung, F. L., 2014. Kernel density estimation, kernel methods, and fast learning in
480 large data sets. IEEE T. Cybern. 44(1), 1-20.
481 Wang, W., Sefiane, K., Duursma, G., Liang, X., Chen, Y., 2019. Void fraction measurement of gas-
482 liquid two-phase flow based on empirical mode decomposition and artificial neural networks. Heat
483 Transf. Eng. 40(16), 1403-1416.
484 Wen, C., Karvounis, N., Walther, J.H., Yan, Y.Y., Feng, Y.Q., Yang, Y., 2019. An efficient approach to
485 separate CO_2 using supersonic flows for carbon capture and storage. Appl. Energ. 238, 311-319.
486 Xie, D., Huang, Z., Ji, H., Li, H., 2006. An online flow pattern identification system for gas-oil two-
487 phase flow using electrical capacitance tomography. IEEE Trans. Instrum. Meas. 55(5): 1833-
488 1838.
489 Zhang, C., Zhang, T., Yuan, C., 2011. Oil holdup prediction of oil–water two phase flow using thermal
490 method based on multiwavelet transform and least squares support vector machine. Expert Syst.
491 Appl. 38(3), 1602-1610.
492 Zhang, W.B., Shao, D., Yan, Y. Liu, S., Wang, T., 2018. Experimental investigations into the transient
493 behaviours of CO_2 in a horizontal pipeline during flexible CCS operations. Int. J. of Greenh. Gas
494 Control 79, 193-199.